LBNL-5671E

ERNEST ORLANDO LAWRENCE
BERKELEY NATIONAL LABORATORY

SEASONAL VARIATION OF CH_4 EMISSIONS FROM CENTRAL CALIFORNIA

Seongeun Jeong, Chuanfeng Zhao, Arlyn E. Andrews, Laura Bianco, James M. Wilczak, Marc L. Fischer

Environmental Energy Technologies Division
Lawrence Berkeley National Laboratory
Berkeley, CA 94720

June 2012

Supported by the U.S. Department of Energy under Contract No. DE-AC02-05CH11231.

Seasonal variation of CH_4 emissions from Central California

Seongeun Jeong[1], Chuanfeng Zhao[1,2], Arlyn E. Andrews[3], Laura Bianco[3,4], James M. Wilczak[3], Marc L. Fischer[1]

[1]Atmospheric Science Department, Environmental Energy Technologies Division, Lawrence Berkeley National Lab, Berkeley, CA, USA

[2]Atmospheric, Earth and Energy Division, Lawrence Livermore National Lab, Livermore, CA, USA

[3]Earth System Research Laboratory, NOAA, Boulder, CO, USA

[4]Cooperative Institute for Research in Environmental Sciences, University of Colorado, Boulder, CO, USA

Corresponding author:

Seongeun Jeong

Atmospheric Science Department

MS 90K-127

1 Cyclotron Rd.

Berkeley, CA 94720 USA

phone: 510-486-7216

email: sjeong@lbl.gov

Keywords: methane, greenhouse gas, emission inventory, atmospheric transport, inverse model

Abstract

We estimate seasonal variations in methane (CH_4) emissions from Central California December 2007 through November 2008 by comparing CH_4 mixing ratios measured at a tall tower with transport model predictions based on a global 1 degree *a priori* CH_4 emissions map (EDGAR32) and a 10 km seasonally varying "California-specific" map, calibrated to state-wide by CH_4 emission totals. Atmospheric particle trajectories and surface footprints are computed using the Weather Research and Forecast (WRF) and Stochastic Time-Inverted Lagrangian Transport (STILT) models. Uncertainties due to wind velocity and boundary layer mixing depth are evaluated using measurements from radar wind profilers. CH_4 signals calculated using the EDGAR32 emission model are larger than those based on the California-specific model, in better agreement with measurements. However, Bayesian inverse analyses using the California-specific and EDGAR32 maps yield comparable annually averaged posterior CH_4 emissions totaling 1.55±0.24 times and 1.84±0.27 times larger than the CA-specific prior emissions respectively, for a region of Central California within approximately 150 km of the tower. If these results are applicable across California, state total CH_4 emissions would account for approximately 9% of state total greenhouse gas emissions. Spatial resolution of emissions within the region near the tower reveal seasonality expected from several biogenic sources but correlations in the posterior errors on emissions from both prior models indicate that the tower footprints do not resolve spatial structure of emissions. This suggests that including additional towers in a measurement network will improve the regional specificity of the posterior estimates.

1. Introduction

Methane (CH_4) is an important greenhouse gas (GHG), playing a significant role in the climate system, with a global warming potential (GWP) relative to CO_2 estimated at 21 (g CO_2eq/ g CH_4) over a 100-year period [*IPCC*, 1995]. Earth's CH_4 has increased by about 150% since 1750 in concentration, and accounts for ~ 25% of the total radiative forcing from all long-lived and globally mixed GHGs [*Hofman et al.*, 2006; *Montzka et al.*, 2011]. Correspondingly, attention has focused on inverse model assessment of global [e.g., *Gimson and Uliasz*, 2003; *Houweling et al.*, 1999; *Miller et al.,* 2008], and regional [e.g., *Kort et al.*, 2008; *Zhao et al.*, 2009] CH_4 sources.

At the regional scale, California currently emits approximately 500 Tg of CO_2 equivalent GHGs, with CH_4 currently estimated to contribute approximately 6% of the total [*California Air Resources Board (CARB)*, 2010]. Because California has committed to an ambitious plan to reduce emissions to 1990 levels by 2020 through Assembly Bill 32 (AB-32), verifying the success of control strategies will require accounting for CH_4 emissions.

Emission inventories and ecosystem models provide valuable estimates of the spatiotemporal distributions of CH_4 emissions from a variety of sources [*Christensen et al.*, 1996; *Potter*, 1997; *Huang et al.*, 1998; *Matthews et al.*, 2000; *Zhang et al.*, 2002; *CARB*, 2010; *Tian et al.*, 2010]. However, it is difficult to evaluate the inventory model performance at regional scales, largely due to the lack of continuous measurements covering large areas over long periods. Long-term measurements are important because

of the strong seasonal dependences of CH_4 emissions from natural wetlands [*Cicerone et al.*, 1983; *Wilson et al.*, 1989; *Mingkui et al.*, 1998], agriculture [*Salas et al.*, 2006; *McMillan et al.*, 2007], and other likely sources. Aircraft measurements provide valuable data for estimating surface CH_4 emissions over short time periods but the high flight expense generally limits long-term monitoring [*Matsueda and Inoue*, 1999; *Wratt et al.*, 2001; *Levin et al.*, 2002; *Gimson and Uliasz*, 2003; *Kort et al.*, 2008]. Flux towers provide long-term direct measurements of surface CH_4 emissions, but only over approximately kilometer scale areas [*Mosier et al.*, 1991; *Hansen et al.*, 1993; *Ball et al.*, 1999; *Alm et al.*, 1999]. Mixing ratio measurements from either towers or space-borne remote sensing can provide continuous long-term measurements, representing larger spatial scales but require inverse techniques to infer emissions [*Simpson et al.*, 1997; *Hein et al.*, 1997; *Houweling et al.*, 1999; *Werner et al.*, 2003; *Manning et al.*, 2003; *Bergamaschi et al.*, 2005; *Zhao et al.*, 2009; *Popa et al.*, 2010].

To date, the seasonal variation in CH_4 emissions from different regions of California has not been quantitatively evaluated. This paper quantifies regional CH_4 emissions from Central California over the course of a year period, representing one of the first analyses of seasonal variation in CH_4 emissions from this mixed urban and rural area. The work expands on an initial study by *Zhao et al.* [2009, ZF09 hereafter] that quantified CH_4 emissions from Central California for a three-month period from October to December 2007. In Section 2 we describe the methods we employed, including atmospheric measurements, *a priori* CH_4 emissions inventories, mesoscale meteorology and trajectory transport modeling, and the Bayesian inverse method, focusing on the modifications from

ZF09. Section 3 describes results, including the seasonal variations in calculated footprints, and the inferred surface emissions of CH_4 from Central California for different regions based on simple correlation analysis and the Bayesian analysis of regional emissions. Section 4 summarizes the results and discusses the implications for CH_4 inverse modeling at the regional scale, highlighting the importance of uncertainty in the spatial distribution of *a priori* emissions and the value of multiple measurement stations.

2. Data and Models

Following ZF09, the Bayesian inversion technique employed in this paper obtains posterior CH_4 emission estimates by scaling spatially distributed *a priori* emissions to minimize the difference between tower-based CH_4 mixing ratios and model predictions. Correspondingly, the data sets used in the inversion technique include tower measurements of CH_4 mixing ratios, *a priori* CH_4 emission maps, trajectories used for CH_4 predictions, modeled meteorology used to drive the transport model and the estimated boundary condition at the edge of the modeling domain.

2.1. Measurements

CH_4 measurements were made at 91 and 483 m above ground level on a tall-tower near Walnut Grove, California (WGC, 121.49°W, 38.27°N, 0 m above sea level), beginning in September 2007. The CH_4 mixing ratios at each height are measured every 15 minutes and averaged into the 3-hour means used in this study. Detailed information about the instrument design is described by ZF09 and will not be repeated here. The measurement accuracy, determined by comparison with time synchronized flask sampling and

laboratory analysis at NOAA, is ~ 1 ppbv CH_4 during periods when variations in the continuous CH_4 measurements are small enough to allow clear comparison with the relatively rapid (~ 1 min) flask sampling. This accuracy is both significantly smaller than the measured variations in CH_4 at the tower site and likely insignificant compared to the uncertainties in model predictions of CH_4 mixing ratio described below.

A subset of the measured data was selected for the inverse analysis based upon a "well-mixed" requirement limiting the vertical gradient in CH_4 mixing ratio. As shown in Figure 1, the seasonal-mean diurnal cycles of CH_4 mixing ratio for air sampled from the 91 and 483 m levels are typically most similar from afternoon to late evening, with differences of ~ 50 ppb in winter and ~ 10 ppb in summer. Data were then selected such that the CH_4 mixing ratio difference between 91 and 483 m fell within the range -1 sd $< (C_{91} - C_{483}) < 3$ sd, where sd is the standard deviation of the difference of the mean cycle between beginning of afternoon and late evening (1200 and 2300 local time). Based on this criteria, between 60 and 90% of the data from the afternoon to late evening time window were retained for the inverse analysis in summer and winter, respectively. For example, the December 2007 to November 2008 data are shown in Figure 2 (upper panel), in which the blue circles indicate the data satisfying well-mixed criteria in this study.

In addition to requiring well-mixed conditions, the data were screened to remove periods with obvious contamination from wild fires that were not included in our emission maps (e.g., forest fires). The summer of 2008 included a period with significant fire activity

based on the report from the California Department of Forestry and Fire Protection (CDFFP) [*CDFFP*, 2008]. To identify the summer 2008 period with potential CH_4 sources due to the fires (that are not present in our inventory), we used CO measurements from an instrument similar to that described in *Potosnak et al.* [1999] in the NOAA tall tower network (http://www.esrl.noaa.gov/gmd/ccgg/towers/). Based on the CO measurements for the period from December 2007 to November 2008, which are shown in Figure 2 (lower panel), we identified and excluded the significant fire events that affected Northern and Central California from June 20th to July 28th, 2008. Because the CO screening is not perfect, we note that lower levels of CH_4 emissions from agricultural and heating related biomass combustion could be present in our posterior emission estimates.

We estimate uncertainties in modeled atmospheric transport using measured planetary boundary layer (PBL) heights retrieved from radar wind profilers located near Sacramento (SAC; 121.42°W, 38.30°N), Chowchilla (CCL; 120.24°W, 37.11°N), Chico (CCO; 121.91°W, 39.70°N), and Livermore (LVR; 121.90°W, 37.71°N). Boundary layer depths were estimated using methods described previously [*Bianco and Wilczak*, 2002; *Bianco et al.*, 2008; *Bianco et al.*, 2011] which can estimate daytime PBL heights from about 150 m to 4000 m with an RMS error of ± 200 m [*Dye et al.*, 1995].

2.2. Prior CH_4 Emission Map

WGC is located in a region containing natural gas fields and wetlands to the West, rice agriculture and natural gas fields to the North, livestock agriculture to the South, and

landfills in the regional landscape. To account for this complexity in the landscape of Central California, we have improved mapping of the spatial distribution of CH_4 emissions. The new maps update the emission maps from ZF09 to more accurately capture the spatial information available to map CH_4 emissions, scaled to the 2008 state-wide sums contained in the CARB CH_4 emission inventory by emissions sector [*CARB*, 2010]. Relevant to the following work, readers should note that the sub-region classification for emission estimates described in ZF09 is shown in Figure 3a. In this section, major improvements for *a priori* emissions over ZF09 are described. First, the spatial distribution of CH_4 emissions from dairy livestock (LS) are improved by using a map of dairy livestock density supplied by the California Department of Water Resources scaled to annual CH_4 emissions assuming a constant emission factor of 0.39 kg C/cow/day from the recent work of *Salas et al.* [2009], resulting in total CH_4 emissions from livestock that are 1.8 times the total livestock emission estimate from ZF09 (Figure 3b).

Second, we identified natural gas wells in California using information from California Department of Conservation (CDC, http://www.consrv.ca.gov/dog/Pages/statistics.aspx) to generate a new emission map from gas wells, which were not accounted for in ZF09. CH_4 emissions from gas wells are estimated using gas production information from CDC [2009]. *Harrison et al.* [1997] estimated CH_4 emissions equivalent to 1.4±0.5% of gross natural gas production for the 1992 baseline year for the entire gas production processes from field production to distribution. Since the available data for this study do not provide detailed information of gas production processes for individual gas fields or

wells, we assumed a leakage rate of 1% related to gas production and transmission/storage processes in the gas fields. CDC Districts 5 and 6 are within the footprint region of WGC. However, the gas production of District 5 is only 5% of that of District 6. Thus, we focus on natural gas emissions from District 6 where most wells produce natural gas only, and total gas production (for 2008) was 2.27×10^9 m^3. Figure 3c shows the resulting CH_4 emission map from natural gas wells. The remaining Districts (1 - 4) in the southern San Joaquin Valley and other locations in Southern California are primarily operated to produce liquid petroleum, but also produce a significant amount of "associated" natural gas. Because the fractional CH_4 leakage rate from the petroleum facilities are likely different from that for the natural gas fields and because the WGC footprints have weak sensitivity to Districts 1 - 4, CH_4 emissions from Districts 1 - 4 are estimated from California mandatory reports on oil and gas. The remainder of natural gas emissions was apportioned by population density in California using 4-km population maps available from the Socioeconomic Data and Applications Center (SEDAC, http://sedac.ciesin.columbia.edu/gpw) [*CIESIN et al.*, 2005] so that the state-wide total estimate from natural gas matched the CARB inventory. Total natural gas emissions based on California population density are shown in Figure 3d.

Third, we used seasonally varying CH_4 emissions for agricultural CH_4 sources. Monthly averaged CH_4 emission maps for county level agricultural CH_4 fluxes were taken from the denitrification and decomposition model (DNDC) output (assuming the 1983, high irrigation case) described by *Salas et al.* [2006]. Wetland CH_4 emissions were taken from monthly averages of the Carnegie-Ames-Stanford-Approach CH_4 (CASA-CH_4) model

from *Potter et al.* [2006]. The resulting maps capture the strong seasonality in these emission sources near the WGC tower. Rice agriculture is concentrated in Region 6 while other regions have negligible emissions from it. Rice agriculture accounts for 46% of the total CH_4 emissions in Region 6 in annual average, with estimated emissions of 0.33, 3.63, 1.08 and 0 Tg CO_2eq yr^{-1} for spring, summer, fall and winter, respectively. Similarly, wetland emissions also show a seasonal variation with summer having the maximum, but represent only 6.7, 2.5, 5.2% of the total CH_4 emissions for Regions 6, 7 and 8, respectively.

Figure 3e shows total CA-specific CH_4 surface emissions with a high resolution (~ 10 km), and the EDGAR 32FT2000 (EDGAR32 hereafter) CH_4 emission map (~ 100 km) [*Olivier et al.*, 2005] is shown in Figure 3f. Seasonal CH_4 emissions for the three regions (6, 7 and 8) near the WGC tower are summarized and compared with the EDGAR32 emissions in Table 1. It is worth noting that the EDGAR32 maps especially give large weight to the San Francisco Bay urban area (Region 7), while the CA-specific map gives more weight to the Central Valley (Regions 6 and 8).

2.3. Trajectory and Meteorology

Predicted contributions to CH_4 mixing ratios from emissions within the modeling domain are calculated as **Fe**, where **F** is footprint strength, and **e** is the *a priori* CH_4 emissions. Footprints are calculated from particle trajectories simulated using the Stochastic Time-Inverted Lagrangian Transport (STILT) model [*Lin et al.*, 2003, 2004]. In this study, 500

particles are released hourly (from UTC hour 00) at the WGC tower (91 m) and transported backward in time 7 days to insure a majority of the particles reach positions representative of the marine boundary layer. The meteorology used to drive this transport model is from the simulation of Weather Research and Forecast (WRF2.2) model [*Skamarock et al.*, 2005]. WRF2.2 has been slightly modified to be coupled with STILT (WRF-STILT) by *Nehrkorn et al.* [2010].

The WRF model simulations follow those described in ZF09 with the following two modifications. First, the PBL scheme was changed from the Yonsei University (YSU) scheme to the Mellor-Yamada-Janjic (MYJ) TKE scheme [*Mellor and Yamada*, 1982; *Janjic*, 1990]. Second, we nested sub-domains using spatial resolutions of 36, 12, and 4 km (shown in Figure 4) at a ratio of 1/3 (rather than 1/5 used in ZF09) to reduce discontinuities, and employed 50 vertical layers between surface and 100 mb to better resolve the planetary boundary layer. Sub-domains were computed with one-way nesting from the next outer sub-region. Each day was simulated separately using 30-hour run (including 6 hours from the previous day for spin-up) with hourly output. And the forecast fields were nudged to the gridded North American Regional Reanalysis (NARR) [*Mesinger et al.*, 2006] fields (32 km resolution) every 3 hours.

2.4. Bayesian Inverse Model

2.4.1. Inversion Approach

We apply a scaling factor Bayesian inversion (SFBI) method to estimate seasonal variations in CH_4 emissions from Central California using measured CH_4 mixing ratios at

a tall tower. As described in *Gerbig et al.* [2003], *Lin et al*. [2003] and ZF09, the local CH_4 mixing ratio at the receptor **c** can be modeled as

$$\mathbf{c} = \mathbf{K}\boldsymbol{\lambda} + \mathbf{v} \qquad (1)$$

where $\mathbf{K} = \mathbf{Fe}$, $\boldsymbol{\lambda}$ is a state vector for scaling factors, which is used to adjust emissions from sources or regions, and **v** is a vector representing the model-data mismatch with a covariance matrix **R**. We model **R** as a diagonal matrix to represent the total variance associated with all error sources such as the measurement error and the transport error. Following the Gaussian assumptions, the posterior estimate for $\boldsymbol{\lambda}$ is

$$\boldsymbol{\lambda}_{post} = \left(\mathbf{K}^T\mathbf{R}^{-1}\mathbf{K} + \mathbf{Q}_{\lambda}^{-1}\right)^{-1}\left(\mathbf{K}^T\mathbf{R}^{-1}\mathbf{c} + \mathbf{Q}_{\lambda}^{-1}\boldsymbol{\lambda}_{prior}\right) \qquad (2)$$

where $\boldsymbol{\lambda}_{\text{prior}}$ is the *a priori* estimate for $\boldsymbol{\lambda}$, and $\mathbf{Q}_{\lambda}$ is the error covariance associated with $\boldsymbol{\lambda}_{\text{prior}}$. Uncertainty associated with total anthropogenic CH_4 emissions in the U.S. ranges from 10% to 50%, and emission uncertainty for rice agriculture is greater than 50% [*Pacala et al.*, 2010]. *Pacala et al.* [2010] also reported that emission estimate uncertainties for manure management and fugitive emissions from fuels are highly variable (less than 10% - 100%). Because the Central California region includes such uncertain CH_4 emission sources as rice agriculture, livestock and natural gas fields, we use 50% uncertainty in our *a priori* emission models for the baseline analysis. The posterior error covariance for $\boldsymbol{\lambda}$ is given by

$$\mathbf{V}_{post} = \left(\mathbf{K}^T \mathbf{R}^{-1} \mathbf{K} + \mathbf{Q}_{\lambda}^{-1}\right)^{-1} \qquad (3)$$

To determine optimal emissions, we use the SFBI method at a monthly temporal scale based on the two CH_4 *a priori* emission models described in Section 2.2. In this paper, however, most of the results are summarized seasonally. We combine May with April and July with June because the number of observations for May and July is much smaller than the other months due to missing data and removal of data from wild fire periods. The inverse modeling approach is applied in two phases as in *Bergamaschi et al.* [2005]. A first inversion is conducted based on the data selected using the well-mixed condition criteria described in Section 2.1. The second (final) inversion uses data points that are accepted by applying the selection criteria $|\mathbf{c}_i - (\mathbf{K}\boldsymbol{\lambda})_i|^2 < \alpha \mathbf{R}_i$, where α is a fixed value for each month. As in the first inversion, the final inversion is performed using the original *a priori* emission maps, and therefore the first inversion is used as a data selection tool for the atmospheric observations. This phased approach removes outliers that might otherwise induce biases in the inversion. *Bergamaschi et al*. [2005] accepted data for α = 2, though they found that relaxing α to 3 had a very small effect on the posterior $\boldsymbol{\lambda}$. In this study, we choose the value of α for each month via an iterative process such that the chi-square values from the final inversion are close to unity [*Tarantola*, 1987]. A sensitivity analysis for α is described in Section 3.4.

2.4.2. Error Covariance Analysis

Following *Gerbig et al.* [2003], ZF09, and *Göckede et al.* [2010], the diagonal elements of the model-data mismatch matrix **R** are estimated from the linear sum of contributing uncertainties in the footprints (e.g., number of particles released, flux aggregation at finite resolution, uncertainties in modeled transport winds and PBL), the estimated CH_4 background, and the *a priori* emissions. Here,

$$\mathbf{R}_i = \mathbf{S}_{part} + \mathbf{S}_{aggr} + \mathbf{S}_{bkgd} + \mathbf{S}_{TransPBL} + \mathbf{S}_{TransWIND}, \qquad (4)$$

where errors are calculated by comparing the root-mean-square (RMS) differences in simulated CH_4 signals. For the particle number error ($\mathbf{S}_{part}$, ~ 5% of background-subtracted mean signal) the comparison is made between test runs releasing 1000 particles and the bulk runs calculated with the release of 500 particles. The aggregation error ($\mathbf{S}_{aggr}$, ~ 11%) is obtained from the comparison made between runs using full (0.1 degree pixel) fluxes and fluxes aggregated to county level.

For the marine background error ($\mathbf{S}_{bkgd}$) the comparison is made between the minimum nighttime CH_4 measured at 483 m (presuming near free troposphere values) and values propagated to the tower from a model of Pacific ocean CH_4 mixing ratios. Following ZF09, we estimated the background CH_4 mixing ratio using the final latitude of each particle as a lookup into the latitudinally averaged marine boundary layer (MBL) CH_4 (NOAA Globalview CH_4 product, http://www.esrl.noaa.gov/gmd/ccgg/globalview/index.html). Only time points for which more than 80% of the particles reached longitudes 1.5 degrees from the coast were

included in the study. To account for seasonal variations in background errors, the RMS difference between the MBL background and the 483 CH_4 measurements was calculated for each season. The RMS difference values were 20.3, 14.7, 16.4 and 24.7 ppb for spring, summer, fall, and winter, respectively. These values are significantly higher than the value of 11.7 ppb obtained previously in ZF09 although the months and years are different.

As described in ZF09, errors due to uncertainties in atmospheric transport are significant. To estimate the uncertainty in predicted CH_4 signals due to errors from modeled PBL heights ($\mathbf{S}_{TransPBL}$) and winds ($\mathbf{S}_{TransWIND}$), we evaluated model errors in winds and PBL heights and then calculated the RMS difference in CH_4 signals obtained from simulations with and without input of an additional stochastic component of wind and PBL errors in STILT.

Extending beyond ZF09, we evaluated PBL heights (*Zi*) at four stations. Figure 5 shows the locations of a nearby (within 8 km of WGC) profiler (SAC), and three more distant profilers near Chowchilla (CCL), Chico (CCO), and Livermore (LVR). Most relevant to the WGC measurements, we compare *Zi* from WRF-STILT with measurements from the SAC profiler for January 2008, April 2008, July 2008, and October 2007, the mid-point months of the winter, spring, summer and fall measurement periods. Assuming the uncertainties in modeled and measured *Zi* are roughly equal, the geometric linear regressions of modeled on measured *Zi* yield regression lines statistically consistent with slopes of 1.00±0.25, 0.86±0.04, 1.01±0.08, and 0.97±0.11 for January, April, July, and

October, respectively. The estimated RMS errors were 415 m, 255 m, 159 m, and 289 m for January, April, July, and October, respectively. Assuming the RMS scatter in predicted versus measured *Zi* can be represented as the sum of squares of measurement uncertainty (~ 200 m, *Dye et al.*, 1995) and WRF-STILT model uncertainty, the RMS error in the WRF-STILT model ranges from very small in summer to near 300 m in winter.

To account for the large seasonal variation in the modeled *Zi*, we conducted an error analysis of *Zi* for January, April, and July following the method in ZF09 while we adopt the error of 24% for October from ZF09. We assumed that the mid-point month of each season represents the total variability of the season. For each season, we perturbed *Zi* by 10% and propagated it through transport simulations. Then we computed CH_4 signals (C_{CH4}) based on the perturbation to estimate their sensitivity to *Zi* (i.e., dC_{CH4}/dZi) as a first order approximation. The dC_{CH4}/dZi values for spring, summer and winter were 0.03, 0.03, and 0.14 ppb m^{-1}, respectively. Due to the large RMS difference between the measured and predicted *Zi*, winter showed the largest sensitivity of CH_4 signals to *Zi* in conjunction with the high mean seasonal CH_4. By applying the inferred RMS error in the WRF-STILT model to dC_{CH4}/dZi as in ZF09, we estimated 6.7, 1.6, 12.3 and 32.0 ppb for errors associated with *Zi* for spring, summer, fall and winter, respectively.

Unlike the model-measurement comparison at the SAC site, PBL heights at some other profilers do show small biases. In April 2008, for example, modeled PBL agrees well with the measurements at CCO (slope = 1.03±0.08), but is lower than the measurements

at CCL (slope = 0.78±0.06) and LVR (slope = 0.77±0.05). To estimate the effect of these biases, we calculated CH_4 signals for WGC with and without perturbing PBL depths at distant sites and found the errors to be small compared to the measured signals because of the relatively weak footprint strength at distant locations.

Uncertainty in modeled CH_4 signals due to errors in modeled winds is estimated using modeled and measured winds for the 127 m height on the WGC tower in the months of January, April, July, and October. RMS model-data differences in U and V wind velocities range from about 2 to 3 m s^{-1}, without significant biases. The RMS errors for the U component were 2.41, 2.66, 3.03, and 2.88 m s^{-1} for January, April, July, and October, respectively. For the V component, the RMS errors were 3.11, 2.41, 2.06, and 2.46 m s^{-1} for the same months. The resulting RMS error in modeled wind was estimated across seasons as 3.7 m s^{-1}. Propagating a random wind component of the velocity error through STILT yielded a typical signal variation of ~ 10 % of the background-subtracted mean CH_4 signal.

Finally, assuming all of the errors from equation 4 are independent, the errors were combined in quadrature to yield a total expected model-data mismatch error and are shown in Table 2 along with the number of observations used in the final inversion. Seasonally estimated model-data mismatch errors are used for all the months belonging to the given season. These errors were used to populate the diagonal elements of **R** in equations 2 - 4. The estimated errors are larger than the estimated error (~ 32% of mean CH_4 signal) in ZF09, largely due to the estimated uncertainty in PBL depth and background mixing ratios, though the seasons and years are different. This will have the

effect of reducing the influence that the measurements have in perturbing the prior emission models.

3. Results

3.1. Footprints

Figure 6 shows the average footprints during well-mixed periods, for spring (March, April, May), summer (June, July, August), fall (September, October, November), and winter (December, January, February). There is a clear seasonal pattern for the distribution of footprints. In summer, the footprints are strongest from the San Francisco Bay area to the west of the WGC tower (henceforth Bay-WGC) due to the dominance of land-ocean winds; in the transition seasons of spring and fall, footprints are stronger from the North Central Valley due to a shift toward north-south winds; in winter, the footprints are strongest in the Central Valley, while the Bay-WGC region is second in terms of footprint influence.

3.2. CH_4 Mixing Ratios

The CH_4 signals measured at 91 m are compared with WRF-STILT predictions of background CH_4 signals in Figure 7 for well-mixed periods. In general, the variability in measured CH_4 is larger in winter than the other seasons, consistent with a recent analysis of the seasonality of maximum boundary layer depths [*Bianco et al.*, 2011], which showed that the boundary layer height reaches its maximum in late-spring months. Correspondingly, spring months had the lowest value (27.83 ppb) for the background-subtracted mean CH_4 during the well-mixed periods, with summer, fall and winter having 31.29, 51.28 and 72.65 ppb, respectively. In addition, the minimum values reasonably

approximate predicted background CH_4 at WGC, showing a smoothly varying seasonality with a maximum centered on winter and a minimum centered on late summer.

3.3. Bayesian Region Analysis

We estimated CH_4 emissions from the different regions in Figure 3a using the SFBI model. As described in Section 2.4, the SFBI is first applied to the data selected based on the well-mixed conditions. The first inversion was performed at a monthly scale to avoid temporal aggregation errors, and a total of 628 observations were used to solve for 130 unknowns. After the first optimization, posterior predicted CH_4 mixing ratios from the inversion of CA-specific emissions were compared with observations and summarized at the seasonal scale. Results using a chi-squared (fitexy) linear regression analysis [*Press et al.*, 1992] yielded fitting slopes (RMS error) of 0.65±0.05 (32 ppb), 0.69±0.14 (26 ppb), 0.79±0.05 (59 ppb), and 0.81±0.05 (66 ppb) for spring, summer, fall, and winter, respectively. The posterior fitting slopes are closer to unity, and the RMS errors are reduced by 19% - 22% compared to the results before optimization where RMS errors were 41, 32, 76, and 82 ppb for spring, summer, fall, and winter, respectively and fitting slopes were low (0.3 – 0.5). This result suggests that the inverse optimization has improved the agreement between the measured and predicted CH_4 signals. However, even after applying the optimized scaling factors, the slopes are still less than unity

To address the residual underestimation in the predicted CH_4 signals, outlier points are removed based on a requirement that the difference between measured and predicted mixing ratios fall within a factor α (e.g., $\alpha = 2$) of the estimated error [*Bergamaschi et*

al., 2005]. In this study α ranges between 1.9 and 3.2 depending on the month, and sensitivity of emission estimates to α values is discussed in Section 3.4.

The outlier removals vary with month, excluding 5 - 25% (mean removal rate = 13.4%) and 0 - 27% (mean = 11.8%) of the data used in the first inversion for the CA-specific and EDGAR32 models, respectively. For both cases, the fraction of data removed was consistent with the 12 - 14% removal rate reported by *Bergamaschi et al.* [2005]. We associate the higher fraction of removed data with the overall low emissions in the CA-specific model and the differences in spatial distribution of CH_4 emissions between the two *a priori* models. These outliers may result from uncaptured errors in transport and background signals in our current modeling system. In terms of emission maps, the likely causes of these outliers include local sources that are not included in the inventory and lack of information on detailed temporal and spatial variations of emissions, in particular near the tower where footprints are strong.

After excluding outliers, the SFBI method is applied as a second inversion, and a total of 544 observations were used to solve for 130 unknowns. Figure 8 shows the regression of posterior predicted on measured CH_4 for the mid-point month of each season using the CA-specific emission model. The resulting χ^2 values were between 0.7 - 1.4 for most of the months except for November ($\chi^2 = 2.0$ with fit slope = 0.98±0.05). Summer months showed slightly lower fitting slopes compared to the other months due to the large model-data mismatch error. Compared with the first inversion results, the seasonal slopes

obtained from the final inversion are also closer to unity, and the reduced RMS errors are 19, 14, 25, and 43 ppb for spring, summer, fall, and winter, respectively. This result demonstrates that the two-step optimization procedure has improved the agreement between the measured and predicted CH_4 signals. Comparing the posterior scaling factors between the first and final inversions (Table 3), the two results are statistically consistent, suggesting that there are few significant differences for individual regions and seasons.

From Table 3, we computed annual average scaling factors of 2.24±0.26, 1.57±0.46, and 1.17±0.38 for Regions 6, 7 and 8, respectively, using the final inversion results. This suggests that CH_4 emissions from Region 6 to the north of WGC (the southern end of the Sacramento Valley) are significantly higher than the CA-specific model in the annual average. The seasonal variation in scaling factor for Region 6 decreases slightly in summer compared to spring and fall, partially diminishing the effect of increased summer-time emissions present in the *a priori* model for rice agriculture. The scaling factors for Region 7 (Bay Area and surrounding urban areas) are also higher than the CA-specific *a priori* model but show small increase in emissions in summer, in partial opposition to the change in Region 6. Scaling factors for Region 8 to the south of WGC (in the Northern San Joaquin Valley) appear approximately consistent with the CA-specific model and show little seasonal variation, though there is a modest increase in winter.

Following the above procedure, we performed similar analyses using EDGAR emission maps. First, we calculated predicted CH_4 signals using two different EDGAR emission

models: EDGAR32 and EDGAR42 (EDGAR version 4.2) [*European Commission JRC and Environmental Assessment Agency*, 2011]. Compared to EDGAR32, EDGAR42 provides emission maps at a much higher resolution (0.1º × 0.1º) than EDGAR32, but the same resolution as that of the CA-specific model. The fitting slopes based on EDGAR42 (0.44 – 0.57) were consistently lower than those of EDGAR32 (0.57 – 0.64) for all seasons. The RMS errors for EDGAR42 (30 – 77 ppb) were also higher than those of EDGAR32 (25 – 72 ppb) for all seasons. This result is due to the fact that the emission sum for Regions 6, 7 and 8 from the EDGAR42 emission maps is lower than that of EDGAR32 by a factor of 0.77. Compared to EDGAR32, EDGAR42 shows little change in the spatial distribution of CH_4 emissions and yields emission sums of 2.62, 5.73, and 3.16 Tg CO_2eq yr^{-1} for Regions 6, 7 and 8, respectively. Compared to the CA-specific model, the emission sum for Region 7 from EDGAR42 is still significantly higher by a factor of 4.48 while the emission sum for Region 8 is lower by a factor of 0.61 (see Table 1). Therefore, in this study we proceed with Bayesian inverse analyses only using EDGAR32 although our future study may reveal more information of the spatial distribution of CH_4 emissions using *a priori* emission models at different spatial scales and distributions.

Figure 9 shows the comparison of posterior predicted and measured CH_4 signals from the final inversion (543 observations) using the EDGAR32 emission model for the mid-point month of each season. The resulting slopes and RMS errors are comparable to the inverse results with the CA-specific model. This result suggests that the EDGAR32 model, used in combination with the measurements from this single tower, provides an equally good

description of CH_4 emissions, despite the fact that the spatial resolution (~ 100 km) is much coarser than that of the CA-specific emission map (~ 10 km). This result also suggests that a combination of the footprints spatial structure and errors in transport and background data do not allow us to distinguish emission estimates from the high-resolution emission maps from those of the low-resolution maps when the emission model with a higher spatial resolution does not influence the inversion result significantly.

Inferred CH_4 emissions are reported by region and as a regional sum over the region (6, 7, and 8) near the tower in Figure 10. Emission sums for the region from the CA-specific emission model based on the 50% uncertainty assumption in the prior are 11.78±2.11, 19.25±2.97, 14.12±2.12, and 11.33±1.54 Tg CO_2eq yr^{-1} (assuming a GWP of 21 g CO_2eq/ g CH_4) for spring, summer, fall, and winter, respectively. However, the EDGAR32 model shows different seasonal emission sums for the region: 16.10±2.24, 13.38±2.04, 19.71±2.30, and 17.98±3.13 Tg CO_2eq yr^{-1}. In particular, the emission sum for winter shows the largest difference. It appears that this discrepancy during winter is due to the difference in the emission distribution between the two prior models. The EDGAR32 model estimates more emissions in Region 7 while the CA-specific model shows more emissions in Region 8 during winter. In Region 6, the EDGAR32 model shows seasonal variation with posterior scaling factors of 0.99±0.12, 1.50±0.20, 1.23±0.17, and 0.86±0.17 for spring, summer, fall, and winter, respectively, but its seasonal variation is much smaller than that of the CA-specific model, which has seasonal components driven by wetland and rice agriculture emissions. For Region 7, the EDGAR32 model shows

the opposite seasonal variation to that of the CA-specific model. The inversion based on the EDGAR32 model yields posterior scaling factors of 0.94±0.22, 0.62±0.14, 1.29±0.23, and 1.28±0.36 for spring, summer, fall, and winter, respectively. Combined with the large emission sum for Region 7 from EDGAR32, which is ~ 6 times that of the CA-specific model, seasonal variation in CH_4 emissions based on EDGAR32 is significantly different from that of the CA-specific case. This difference between the two models will be discussed more in terms of correlations between regions. For Region 8, seasonal variation from the EDGAR32 model is small as was the case with the CA-specific model.

We then investigated the degree to which the tower footprints allow spatial resolution of emissions between the different sub-regions by considering the off-diagonal elements of the posterior error covariance matrices and *a priori* emission model. In this regard, as *Tarantola* [1987] suggested, we derive correlations from the posterior covariance rather than a direct examination of the off-diagonal elements of the covariance. The correlations, which vary each month due to changing footprints, were generally negative between Regions 6 and 7 for both CA-specific (-0.1 to -0.4) and EDGAR models (-0.2 to -0.8). The correlations between Regions 6 and 8 were also negative for both CA-specific (-0.1 to -0.6) and EDGAR32 (-0.1 to -0.5) cases. It is worth noting that for the EDGAR32 case the anti-correlation is much stronger in Regions 6 – 7 than in Regions 6 – 8. It appears that this stronger anti-correlation in Region 6 – 7 occurs when the EDGAR emission sum for Region 7, which is 2.7 times that of Region 8, is adjusted against Region 6 via the inversion system. This suggests that roughly 10 - 40% of emissions attributed to Region 6 in the CA-specific emission model could be traded off against

emissions from Region 7 and vice versa. This result further suggests that our inversion system has not solved the scaling factors entirely in an independent manner and only some linear combination of those scaling factors may be resolved.

3.4. Sensitivity Analysis

A sensitivity analysis of prior uncertainty was conducted to investigate its impact on CH_4 emission estimates. With the 50% prior uncertainty as the baseline, we performed inversions using 70% and 90% prior uncertainties in the *a priori* emission models. The results showed that there is no significant change in CH_4 region sum estimates with different uncertainties in either the CA-specific or EDGAR model. For the CA-specific case, the region sums based on the 90% uncertainty case were 12.94±3.18, 20.97±4.95, 14.94±3.05, and 13.70±2.24 Tg CO_2eq yr^{-1} for spring, summer, fall, and winter, respectively, which are not significantly different from the 50% uncertainty case: 11.78±2.11, 19.25±2.97, 14.12±2.12, and 11.33±1.54 Tg CO_2eq yr^{-1}. Emissions from 70% uncertainty ranged between these two results, showing no significant change in CH_4 emission estimates. The EDGAR-based inversion also showed no significant difference in the region sum for each season among different prior uncertainty assumptions.

In addition to the prior uncertainty sensitivity analysis, we performed a sensitivity analysis on the observation period using observational data during the afternoon hours (1200 – 1700 local) as a subset of the original data. In this inversion, the number of 3-hourly observations is 284 while the number of unknowns is 130 as in the case of the original inversion. Based on the 50% uncertainty assumption in the *a priori* emission

map, the final inversion using the CA-specific emission model yielded emission sums of 12.12±2.47, 20.30±3.12, 17.55±2.61, and 12.83±1.78 Tg CO_2eq yr^{-1} for spring, summer, fall, and winter. Compared to those of the original inversion, we find that there is no significant difference between the two inverse analyses.

We also conducted a sensitivity analysis on the α value used to remove outliers for the final inversion. We repeated the inversion using a fixed value of 2 for α instead of using varying values depending on the χ^2 statistic. In this inversion, the number of 3-hourly observations is 516, which is slightly smaller than 544 observations used in the original analysis. As *Bergamaschi et al.* [2005] indicated, the difference between the two analyses was small. The case based on the fixed value of 2 yields emissions sums of 11.12±2.12, 19.49±2.96, 14.84±2.27, 10.93±1.73 Tg CO_2eq yr^{-1} for spring, summer, fall, and winter, respectively, which are very similar to those of the case with varying α.

Finally, 2008 included a period with significant fire activities and the data were initially screened to remove periods with obvious contamination from wild fires as described in Section 2.1. We also investigated the sensitivity of emission estimates to the fire activities. When observations from the summer fire periods were not removed, the final inversion yielded a region sum of 19.90±2.96 Tg CO_2eq yr^{-1} for Regions 6, 7 and 8 during the summer season, which does not deviate significantly from 19.25±2.97 Tg CO_2eq yr^{-1} of the original inversion. The inversion with the fire periods included showed 11.33±1.20, 2.65±0.57, and 5.92±2.65 Tg CO_2eq yr^{-1} for Regions 6, 7 and 8, respectively.

This result is also comparable to 11.20±1.21, 2.48±0.57, and 5.57±2.65 Tg CO_2eq yr^{-1} from the original analysis.

4. Discussion

The regionally summed annual posterior CH_4 emissions are 14.12±2.19 and 16.79±2.43 Tg CO_2eq for the CA-specific and EDGAR32 models, larger than the sum of the CA-specific prior (9.13 Tg CO_2eq) by factors of 1.55±0.24 and 1.84±0.27, respectively. The similarity of these two factors suggests that inferred emissions for the area within approximately 150 km of the tower are independent of the two emission models and that actual summed CH_4 emissions are significantly higher than the sum inferred from the CARB inventory. In terms of the spatial distribution of CH_4 emissions, these results indicate that the inversion system constrains emissions somewhat independent of the resolution of the emission map. Assuming these average posterior scaling factors were applicable to all regions of California, the resulting total CH_4 emissions would comprise approximately 9% of total GHG emissions, a result that requires further investigation and confirmation [*CARB*, 2010].

The CA-specific *a priori* model shows clear seasonal variations in total CH_4 emissions, producing significantly greater total emissions in summer, moderate emissions in fall, and lower emissions in winter and spring. The higher summer-time emissions are concentrated in Region 6, a result that is consistent with the spatial distribution and seasonality of the *a priori* emissions from rice agriculture [*Salas et al.*, 2006]. This

provides consistent evidence for increased emissions in summer as expected in biological systems responding to warmer temperatures such as rice and wetlands [*Potter et al.*, 2006; *McMillan et al.,* 2007]. On the contrary, posterior emissions obtained with the EDGAR model yield only weak seasonality in total CH_4 emissions for the three regions although the fall and winter emissions are marginally different from those of the other seasons. In particular, the high winter emissions from the EDGAR model are likely due to a combination of urban emissions in the *a priori* model (i.e., ~ six times larger than that of the CA-specific model), its coarse spatial resolution, and weak footprints in the urban region during winter. It is conceivable that emissions from Region 7 might increase in winter due to urban emission sources such as increased natural gas use. However, it seems unlikely that natural gas emissions from Region 7 could drive the seven-fold increase in posterior emissions (10.47±2.95 Tg CO_2eq yr^{-1}) compared to that (1.56±0.62 Tg CO_2eq yr^{-1}) of the CA-specific model, considering that natural gas accounts for only less than 30% of the total emission in Region 7. A further study is required to resolve this discrepancy, possibly using more measurements from multiple stations combined with additional improvements in *a priori* emission models.

As described above, it appears that the different emissions models combined with the time varying footprints produce posterior emission sums that 1) peak in different regions and seasons, and 2) contain anti-correlations among regions which limit unique spatial attribution of emissions. This type of anti-correlation in posterior emission estimates for different regions has been reported in the inversion results of *Bergamaschi et al.* [2005], and suggests that a network of measurement stations will be required to accurately

resolve the spatial distributions of CH_4 emissions over the state of California [*Fischer et al.,* 2009].

Acknowledgements

We thank Dave Field, Dave Bush, Edward Wahl, and particularly Jon Kofler for assistance with installation and maintenance of the instrumentation at WGC, Edward Dlugokencky for advice and assistance in verifying the Picarro instrument performance at NOAA, John Lin, Steve Wofsy, Janusz Eluszkiewicz and Thomas Nehrkorn for generously sharing the STILT code and providing advice, Chris Potter and William Salas for sharing modeled CH_4 emission for use as *a priori* estimates, Larry Hunsaker and Webster Tassat for providing the CARB estimates of landfill CH_4 emissions, and Krishna Muriki for assistance running WRF-STILT on the LBNL-Lawrencium computer cluster. We gratefully acknowledge NOAA Air Resources Laboratory (ARL) for the use of the HPSPLIT model underlying STILT, and NCEP for the provision of the NARR meteorology. We also thank Jean Bogner, Eric Crosson, Guido Franco, Ying-Kuang Hsu, Eileen McCauley, and Tony VanCuren for valuable comments. This study was supported by the California Energy Commission (CEC) Public Interest Environmental Research Program and the Director, Office of Science, Office of Basic Energy Sciences, of the U.S. Department of Energy under Contract No. DE-AC02-05CH11231. The contribution of Chuanfeng Zhao for this work was partly performed under the auspices of the U. S. Department of Energy by Lawrence Livermore National Laboratory under contract DE-AC52-07NA27344. The findings, views, and opinions presented in this paper do not necessarily represent the views and opinions of the California Energy Commission or the State of California.

References

Alm, J., S. Saarnio, H. Nykanen, J. Silvola, and P. J. Martikainen (1999), Winter CO_2, CH_4, and N_2O fluxes on some natural and drained boreal peatlands, *Biogeochem.*, **44**, 163-186.

Ball, B. C., A. Scott, and J. P. Parker (1999), Field N_2O, CO_2 and CH_4 fluxes in relation to tillage, compaction and soil quality in Scotland, *Soil Tillage Res.*, **53(1)**, 29-39.

Bergamaschi, P., M. Krol, F. Dentener, A. Vermeulen, F. Meinhardt, R. Graul, M. Ramonet, W. Peters, and E. J. Dlugokencky (2005), Inverse modelling of national and European CH_4 emissions using the atmospheric zoom model TM5, *Atmos. Chem. Phys.*, **5**, 2431–2460.

Bianco, L., and J. M. Wilczak (2002), Convective boundary layer depth: Improved measurement by Doppler radar wind profiler using fuzzy logic methods, *J. Atmos. Ocean. Technol.*, **19**(11), 1745-1758.

Bianco, L., J. M. Wilczak, and A. B. White (2008), Convective boundary layer depth estimation from wind profilers: Statistical comparison between an automated algorithm and expert estimations, *J. Atmos. Ocean. Tech.*, **25**, 1397-1413.

Bianco, L., I. V. Djalalova, C. W. King, and J. M. Wilczak (2011), Diurnal evolution and annual variability of boundary-layer height and its correlation to other meteorological variables in California's Central Valley, *Boundary-Layer Meteorology*, **140**, 491-511, DOI 10.1007/s10546-011-9622-4, 1-21.

CARB (2010), California Greenhouse Gas Emission Inventory, California Air Resources Board Staff Report. (http://www.arb.ca.gov/cc/inventory/inventory.htm)

California Department of Conservation (2009), 2008 Annual Report of the State Oil and Gas Supervisor. Publication No. PR06. (http://www.conservation.ca.gov/dog/pubs_stats/annual_reports/Pages/annual_reports.aspx)

California Department of Forestry and Fire Protection (2008), All statewide fires from 6/22/08 to 8/11/08. (http://www.fire.ca.gov/downloads/incidents/All_statewide_Fires_0622_081108_a.pdf)

Center for International Earth Science Information Network (CIESIN), Columbia University, and Centro Internacional de Agricultura Tropical (CIAT) (2005), Gridded Population of the World, Version 3 (GPWv3): Population Density Grid. Palisades, NY: Socioeconomic Data and Applications Center (SEDAC), Columbia University. (http://sedac.ciesin.columbia.edu/gpw)

Christensen, T. R., I. C. Prentice, J. Kaplan, A. Haxeltine, and S. Sitch (1996), Methane flux from northern wetlands and tundra: An ecosystem source modeling approach, *Tellus B*, **48** (5), 652-661.

Cicerone, R. J., J. D. Shetter, and C. C. Delwiche (1983), Seasonal variation of methane flux from a California rice paddy, *J. Geophy. Res.*, **88**, 11022-11024.

Dye, T.S., C. G. Lindsey, and J. A. Anderson (1995), Estimates of mixing depth from "boundary layer" radar profilers. *Preprints from the 9th Symposium on Meteorological Observations and Instrumentation*, Charlotte, NC, March 27-31, 156-160 (STI-94212-1451).

European Commission, Joint Research Centre (JRC)/Netherlands Environmental Assessment Agency (2011), Emission Database for Global Atmospheric Research (EDGAR), release version 4.2. (http://edgar.jrc.ec.europa.eu)

Fischer, M. L., C. Zhao, W. J. Riley, and A. C. Andrews (2009), *Observation of methane and other non-carbon dioxide greenhouse gas emissions from California.* California Energy Commission, PIER Energy-Related Environmental Research. CEC-500-2009-096.

Gerbig, C, J. Lin, S. Wofsy, B. Daube, A. E. Andrews, B. Stephens, P. S. Bakwin, and C. Grainger (2003), Toward constraining regional-scale fluxes of CO_2 with atmospheric observations over a continent: 2. Analysis of COBRA data using a receptor-oriented framework, *J. Geophys. Res.*, **108**(D24), 10.1029/2003JD003770.

Gimson, N. R. and M. Uliasz (2003), The determination of agricultural methane emissions in New Zealand using receptor-oriented modelling techniques, *Atmos. Environ.*, **37**, 3903-3912.

Göckede , M., A. M. Michalak, D. Vickers, D. P. Turner, and B. E. Law (2010), Atmospheric inverse modeling to constrain regional-scale CO_2 budgets at high spatial and temporal resolution, *J. Geophys. Res.*, **115**, D15113, doi:10.1029/2009JD012257.

Hansen, S., J. E. Maehlum, and L. R. Bakken (1993), N_2O and CH_4 fluxes in soil influenced by fertilization and tractor traffic, *Soil Biol. Biochem.*, **25**(5), 621-630.

Harrison, M. R., T. M. Shires, J. K. Wessels, and R. M. Cowgill (1997), Methane emissions from the natural gas industry, EPA/600/SR-96/080.

Hein, R., P. J. Crutzen, and M. Heimann (1997), An inverse modeling approach to investigate the global atmospheric methane cycle, *Global Biogeochem. Cycles,* **11**(1), 43–76.

Hofman, D. J., J. H. Butler, E. J. Dlugokencky, J. W. Elkins, K. Masarie, S. A. Montzka, and P. Tans (2006), The role of carbon dioxide in climate forcing from 1979 - 2004: Introduction of the Annual Greenhouse Gas Index, *Tellus B,* **58B**, 614-619.

Houweling, S., T. Kaminski, F. Dentener, J. Lelieveld, and M. Heimann (1999), Inverse modeling of methane sources and sinks using the adjoint of a global transport model, *J. Geophys. Res.*, **104**(D21), 26137-26160.

Huang, Y., R. L. Sass, and F. M. Fisher (1998), A semi-empirical model of methane emission from flooded rice paddy soils, *Global Change Biology*, **4**, 247-268.

IPCC (1995), IPCC Second Assessment Report (SAR), "Climate Change 1995".

Janjic, Z. I. (1990), The step-mountain coordinate: physical package, *Mon. Weather Rev.*, **118**, 1429–1443.

Kort, E. A., J. Eluszkiewicz, B. B. Stephens, J. B. Miller, C. Gerbig, T. Nehrkorn, B. C. Daube, J. O. Kaplan, S. Houweling, and S. C. Wofsy (2008), Emissions of CH_4 and N_2O over the United States and Canada based on a receptor-oriented modeling framework and COBRA-NA atmospheric observations, *Geophy. Res. Lett.*, **35***,* L18808, doi:10.1029/2008GL034031.

Levin, I., P. Ciais, R. Langenfelds, M. Schmidt, M. Ramonet, K. Sidorov, N. Tchebakova, M. Gloor, M. Heimann, E. D. Schulze, N. N. Vygodskaya, O. Shibistova, and J. Lloyd (2002), Three years of trace gas observations over the

EuroSiberian domain derived from aircraft sampling – a concerted action, *Tellus B*, **54**, 696-712.

Lin, J. C., C. Gerbig, S. C. Wofsy, A. E. Andrews, B. C. Daube, K. J. Davis, and C. A. Grainger (2003), A near-field tool for simulating the upstream influence of atmospheric observations: The Stochastic Time-Inverted Lagrangian Transport (STILT) model, *J. Geophys. Res.*, **108**(D16), 4493, doi:10.1029/2002JD003161.

Lin, J. C., C. Gerbig, S. C. Wofsy, A. E. Andrews, B. C. Daube, C. A. Brainger, B. B. Stephens, P. S. Bakwin, and D. Y. Hollinger (2004), Measuring fluxes of trace gases at regional scales by Lagrangian observations: Application to the CO_2 Budget and Rectification Airborne (COBRA) study, *J. Geophys. Res.* **109**, D15304, doi:10.1029/2004JD004754.

Manning, A. J., D. B. Ryall, R. G. Derwent, P. G. Simmonds, and S. O'Doherty (2003), Estimating European emissions of ozone-depleting and greenhouse gases using observations and a modeling back-attribution technique, *J. Geophys. Res.*, **108** (D14), 4405, doi: 10.1029/2002JD002312.

Matsueda, H., and H. Y. Inoue (1999), Aircraft measurements of trace gases between Japan and Singapore in October of 1993, 1996, and 1997, *Geophys. Res. Lett.*, **26**(16), 2413–2416, doi:10.1029/1999GL900089.

Matthews, R. B., R. Wassmann, and J. Arah (2000), Using a crop/soil simulation model and GIS techniques to assess methane emissions from rice fields in Asia. I. Model Development, *Nutr. Cycl. Agroecosyst.*, **58**, 141-159.

McMillan, A. M. S., M. L. Goulden, and S. C. Tyler (2007), Stoichiometry of CH_4 and CO_2 flux in a California rice paddy, *J. Geophys. Res.*, **112**, G01008, doi:10.1029/2006JG000198.

Mellor G. L., and T. Yamada (1982), Development of a turbulence closure model for geophysical fluid problems, *Rev. Geophys. Space Phys.* **20**, 851–875.

Mesinger, F., et al. (2006), North American Regional Reanalysis, *Bull. Amer. Meteor. Soc*., **87** (3), 343-360.

Miller, S. M., et al. (2008), Sources of carbon monoxide and formaldehyde in North America determined from high-resolution atmospheric data, *Atmos. Chem. Phys.*, **8**, 7673-7696.

Mingkui, C., K. Gregson, and S. Marshall (1998), Global methane emission from wetlands and its sensitivity to climate change, *Atmos. Environ.*, **32**(19), 3293-3299.

Montzka, S. A., E. J. Dlugokencky, and J. H. Butler (2011), Non-CO_2 greenhouse gases and climate change, *Nature*, **476**, 43-50, doi:10.1038/nature10322.

Mosier, A., D. Schimel, D. Valentine, K. Bronson, and W. Parton (1991), Methane and nitrous oxide fluxes in native, fertilized and cultivated grasslands, *Nature*, **350**, 330-332.

Nehrkorn, T., J. Eluszkiewicz, S. C. Wofsy, J. C. Lin, C. Gerbig, M. Longo, and S. Freitas (2010), Coupled weather research and forecasting - stochastic time-inverted lagrangian transport (WRF-STILT) model, *Meteor. Atmos. Phys.*, **107** (1), 51-64, doi:10.1007/s00703-010-0068-x.

Olivier, J. G. J., J. A. Van Aardenne, F. Dentener, L. Ganzeveld, and J. A. H. W. Peters (2005), Recent trends in global greenhouse gas emissions: Regional trends and spatial distribution of key sources, in *Non-CO_2 Greenhouse Gases (NCGG-4)*, edited by A. van Amstel, pp. 325–330, Millpress, Rotterdam, Netherlands.

Pacala, S. W., C. Breidenich, P. G. Brewer, I. Y. Fung, M. R. Gunson, G. Heddle, B. E. Law, G. Marland, K. Paustian, M. Prather, J. T. Randerson, P. P. Tans, and S. C. Wofsy (2010), *Verifying greenhouse gas emissions: Methods to support international climate agreements*, Committee on Methods for Estimating Greenhouse Gas Emissions, National Research Council.

Popa, M. E., M. Gloor, A. C. Manning, A. Jordan, U. Schultz, F. Haensel, T. Seifert, and M. Heimann (2010), Measurements of greenhouse gases and related tracers at Bialystok tall tower station in Poland, *Atmos. Meas. Tech.*, **3**, 407-427.

Potosnak, M. J., S. C. Wofsy, A. S. Denning, T. J. Conway, J. W. Munger, and D. H. Barnes (1999), Influence of biotic exchange and combustion sources on atmospheric concentrations in New England from observations at a forest flux tower, *J. Geophys. Res.*, **104**(D8), 9561-9569.

Potter, C. S. (1997), An ecosystem simulation model for methane production and emission from wetlands, *Global Biogeochem. Cycles*, **11**(4), 495–506, doi:10.1029/97GB02302.

Potter, C., S. Klooster, S. Hiatt, M. Fladeland, V. Genovese, and P. Gross (2006), Methane emissions from natural wetlands in the United States: Satellite-derived estimation based on ecosystem carbon cycling. *Earth Interactions*, **10**, 1–12.

Press, W. H., S. A.Teukolsky, W. T. Vetterling, and B.P. Flannery (1992), *Numerical Recipes, 2nd edition*. Cambridge: Cambridge University Press.

Salas, W., P. Green, S. Frolking, C. Li, and S. Boles (2006), *Estimating Irrigation Water Use for California Agriculture: 1950s to Present*, California Energy Commission, PIER Energy-Related Environmental Research, CEC-500-2006-057.

Salas, W., C. Li, F. Mitloehner, and J. Pisano (2009), *Developing and Applying Proces based Models for Estimating GHG and Air Emission from California Dairies*, California Energy Commission, PIER Energy-
Related Environmental Research, CEC-500-2008-093.

Simpson, I. J., G. C. Edwards, G. W. Thurtell, G. den Hartog, H. H. Neumann, and R. M. Staebler (1997), Micrometeorological measurements of methane and nitrous oxide exchange above a boreal aspen forest, *J. Geophys. Res.*, **102**(D24), 29,331–29,341, doi:10.1029/97JD03181.

Skamarock, W. C., J. B. Klemp, J. Dudhia, D. O. Gill, D. M. Barker, W. Wang, and J. G. Powers (2005), A description of the advanced research WRF version 2. *Technical Note 468*+STR, MMM Division, NCAR, Boulder, CO.

Tarantola, A. (1987), *Inverse Problem Theory Methods for Data Fitting and Model Parameter Estimation*, 613 pp., Elsevier, New York.

Tian, H., X. Xu, M. Liu, W. Ren, C. Zhang, G. Chen, and C. Lu (2010), Spatial and temporal patterns of CH_4 and N_2O fluxes in terrestrial ecosystems of North America during 1979-2008: application of a global biogeochemistry model, *Biogeosciences,* **7**(9), 2673-2694.

Werner, C., K. Davis, P. Bakwin, C. Yi, D. Hurst, and L. Lock (2003), Regional-scale measurements of CH_4 exchange from a tall tower over a mixed temperate/boreal lowland and wetland forest, *Global Change Biol.*, **9**, 1251-1261.

Wilson, J. O., P. M. Crill, K. B. Bartlett, D. I. Sebacher, R. C. Harriss, and R. L. Sass (1989), Seasonal variation of methane emissions from a temperature swamp, *Biogeochemistry*, **8**, 55-71.

Wratt, D. S., N. R. Gimson, G. W. Brailsford, K. R. Lassey, A. M. Bromley, and M. J. Bell (2001), Estimating regional methane emissions from agriculture using aircraft measurements of concentration profiles, *Atmos. Environ.*, **35**, 497-508.

Zhang Y., C. Li, X. Zhou, and B. Moore (2002), A simulation model linking crop growth and soil biogeochemistry for sustainable agriculture, *Ecol. Modell.*, **151**, 75-108.

Zhao, C., A. E. Andrews, L. Bianco, J. Eluszkiewicz, A. Hirsch, C. MacDonald, T. Nehrkorn, and M. L. Fischer (2009), Atmospheric inverse estimates of methane emissions from Central California, *J. Geophys. Res.*, **114**, D16302, doi:10.1029/2008JD011671.

Figure captions

Figure 1. Diurnal cycles of mean hourly (PST) measured CH_4 mixing ratio obtained for 91 and 483 m sampling heights on the WGC tower for the period from December 2007 to November 2008.

Figure 2. Tower measurements of CH_4 (top panel) and CO (bottom panel) at 91 m (black) and 483 m (red) as functions of date (expressed as day/month) for the period between December 2007 and November 2008. The blue circles indicate the data satisfying the well-mixed criteria in this study. The vertical bars indicate the fire period from June 20 to July 28, 2008, which was excluded from further analysis.

Figure 3. (a) Region classifications, and *a priori* CH_4 emissions from (b) livestock, (c) natural gas wells, (d) natural gas based on California population density, (e) the total CA-specific emission model, and (f) the EDGAR32 emission model. The location of the tower is marked with an "x" near longitude = 121ºW, latitude = 38ºN. The triangle in (c) represents the location of the Rio Vista Gas (RVG), which is one of the largest gas fields in California.

Figure 4. WRF initial boundary set up with three-level nested domains. The ratio of spatial resolution between the three levels is 3. The resolutions for d01, d02, d03 and d04 are 36, 12, 4 and 4 km, respectively.

Figure 5. Map of Central California showing the location of Walnut Gove Tower (WGC; red "x") and the locations of the four radar wind profilers (black triangles) at Sacramento (SAC), Chico (CCO), Chowchilla (CCL) and Livermore (LVR), with predicted monthly mean PBL heights (m) for June 2008, 10:00 PST shown in color.

Figure 6. Seasonally averaged footprint maps over well-mixed periods for spring (MAM), summer (JJA), fall (SON), and winter (DJF).

Figure 7. Time series (dates given as DD/MM) of measured CH_4 signals (black) and predicted background (red) CH_4 signals at 91 m on the WGC tower for well-mixed periods between December 1, 2007 and November 30, 2008.

Figure 8. Comparison of CH_4 mixing ratios between measurements and predictions based on the final inverse optimization using CA-specific emissions for the mid-point month of (a) spring, (b) summer, (c) fall, and (d) winter. For summer, June and July mixing ratios are compared together due to data removal during fire periods.

Figure 9. Comparison of CH_4 mixing ratios between measurements and predictions based on the final inverse optimization using EDGAR32 emissions for the mid-point month of (a) spring, (b) summer, (c) fall, and (d) winter. For summer, June and July mixing ratios are compared together due to data removal during fire periods.

Figure 10. Comparison of posterior CH_4 emissions (Tg CO_2eq yr^{-1}, assuming a 100-year GWP = 21) by region between the (a) CA-specific and (b) EDGAR32 emission models.

Tables

Table 1. *A Priori* Emissions (Tg CO_2eq yr^{-1}; assuming a GWP of 21 g CO_2eq/ g CH_4) from the CA-specific and EDGAR32 Models for the Three Regions near the WGC Tower

Regions	CA-specific Seasonal				CA-specific Annual	EDGAR32
	Winter	Spring	Summer	Fall		
R06	1.35	1.70	5.13	2.59	2.69	3.59
R07	1.27	1.27	1.30	1.29	1.28	8.22
R08	5.02	5.01	5.33	5.25	5.15	3.10
Total	7.64	7.98	11.76	9.13	9.13	14.90

Table 2. Estimated Model-data Mismatch Errors and Number of Observations for Final Inversions

Month	1	2	3	4 – 5[a]	6 – 7[a]	8	9	10	11	12
Model-data mismatch (ppb)	42.0	42.0	21.8	21.8	15.6	15.6	22.0	22.0	22.0	42.0
Number of observations for CA-specific	36	41	60	87	67	53	60	43	44	53
Number of observations for EDGAR32	35	42	57	88	68	58	62	42	43	48

[a]Data for May and July are combined with those of April and June, respectively, due to missing measurements and fire period cuts.

Table 3. Comparison of Posterior Scaling Factors between First and Final (second) Inversions for Each Season Based on the CA-specific Emission Model

Region	Spring		Summer		Fall		Winter	
	First	Final	First	Final	First	Final	First	Final
R06	2.61±0.25	2.52±0.27	2.25±0.19	2.18±0.24	2.56±0.20	2.58±0.24	1.83±0.29	1.69±0.31
R07	2.20±0.45	1.60±0.46	2.48±0.42	1.91±0.44	2.52±0.45	1.53±0.47	1.76±0.48	1.23±0.49
R08	1.05±0.39	1.09±0.40	1.07±0.50	1.05±0.50	0.84±0.33	1.04±0.37	1.63±0.26	1.49±0.27

Figures

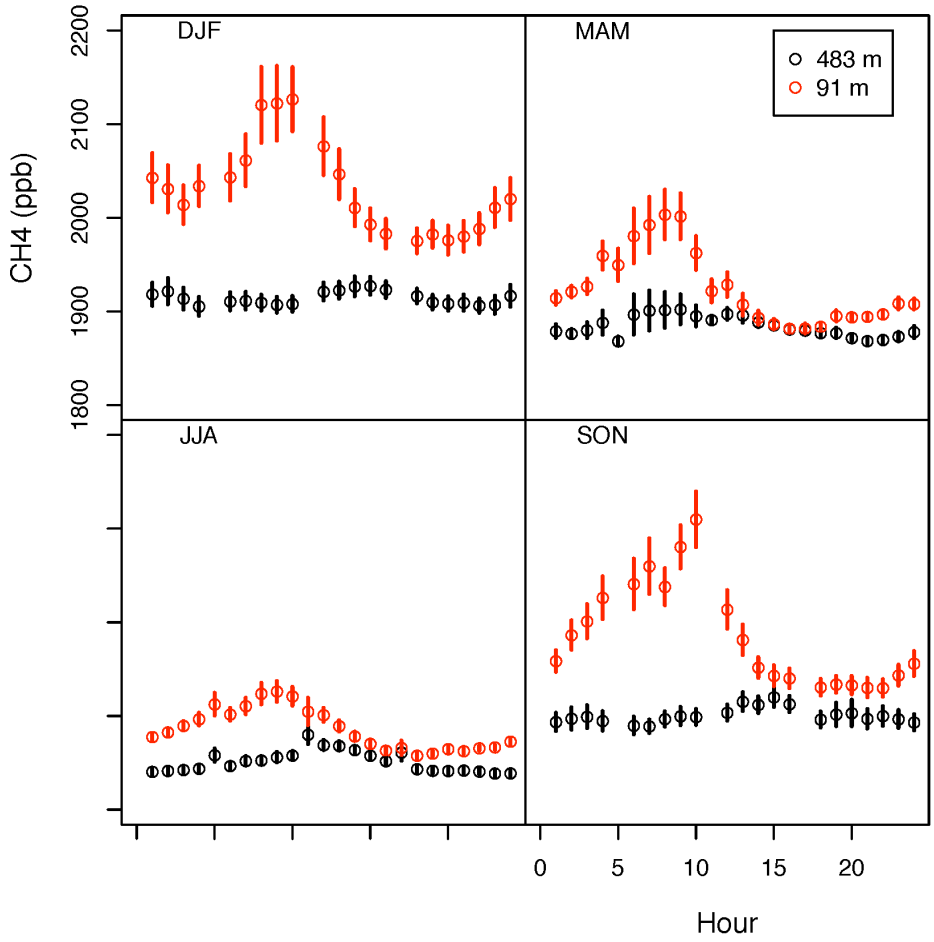

Figure 1. Diurnal cycles of mean hourly (PST) measured CH_4 mixing ratio obtained for 91 and 483 m sampling heights on the WGC tower for the period from December 2007 to November 2008.

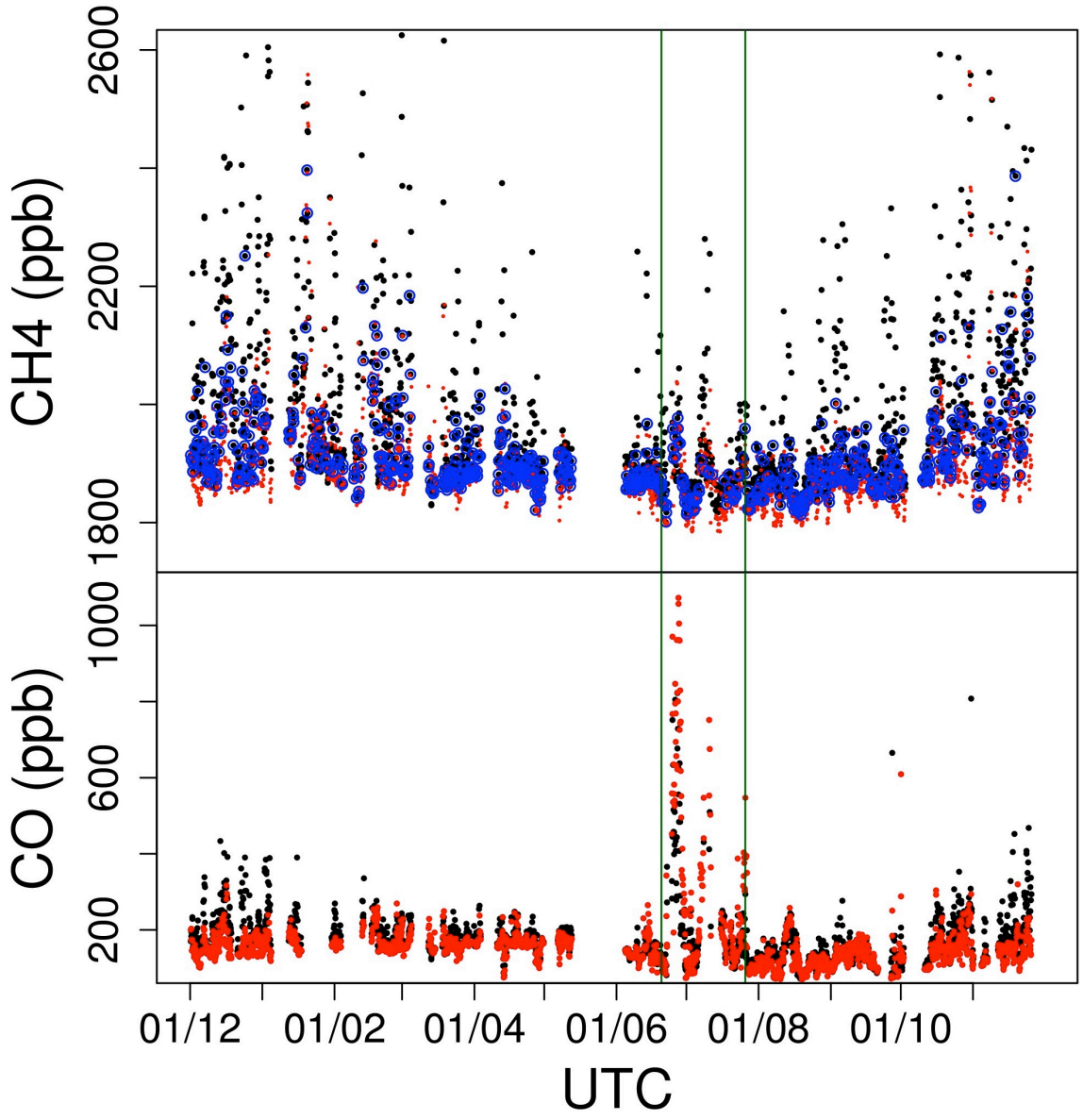

Figure 2. Tower measurements of CH_4 (top panel) and CO (bottom panel) at 91 m (black) and 483 m (red) as functions of date (expressed as day/month) for the period between December 2007 and November 2008. The blue circles indicate the data satisfying the well-mixed criteria in this study. The vertical bars indicate the fire period from June 20 to July 28, 2008, which was excluded from further analysis.

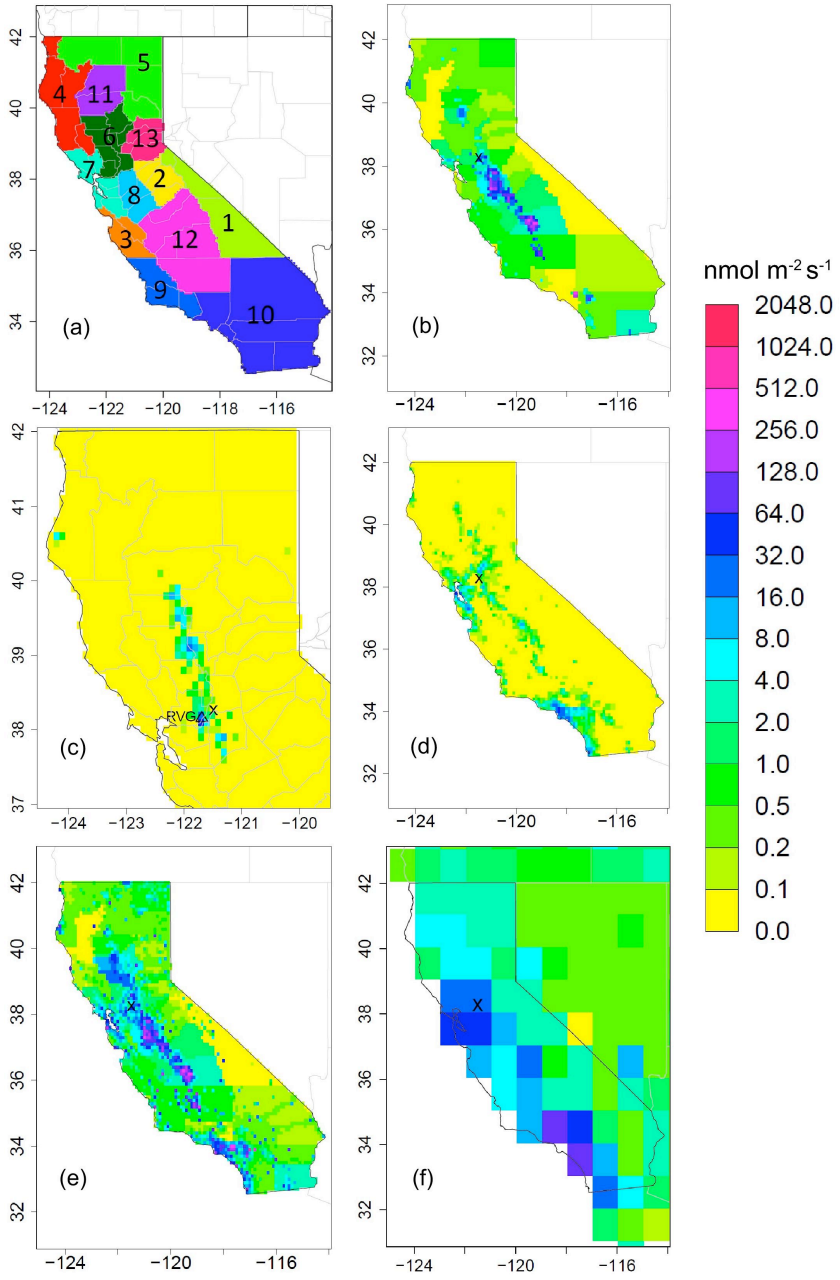

Figure 3. (a) Region classifications, and *a priori* CH_4 emissions from (b) livestock, (c) natural gas wells, (d) natural gas based on California population density, (e) the total CA-specific emission model, and (f) the EDGAR32 emission model. The location of the tower is marked with an "x" near longitude = 121ºW, latitude = 38ºN. The triangle in (c) represents the location of the Rio Vista Gas (RVG), which is one of the largest gas fields in California.

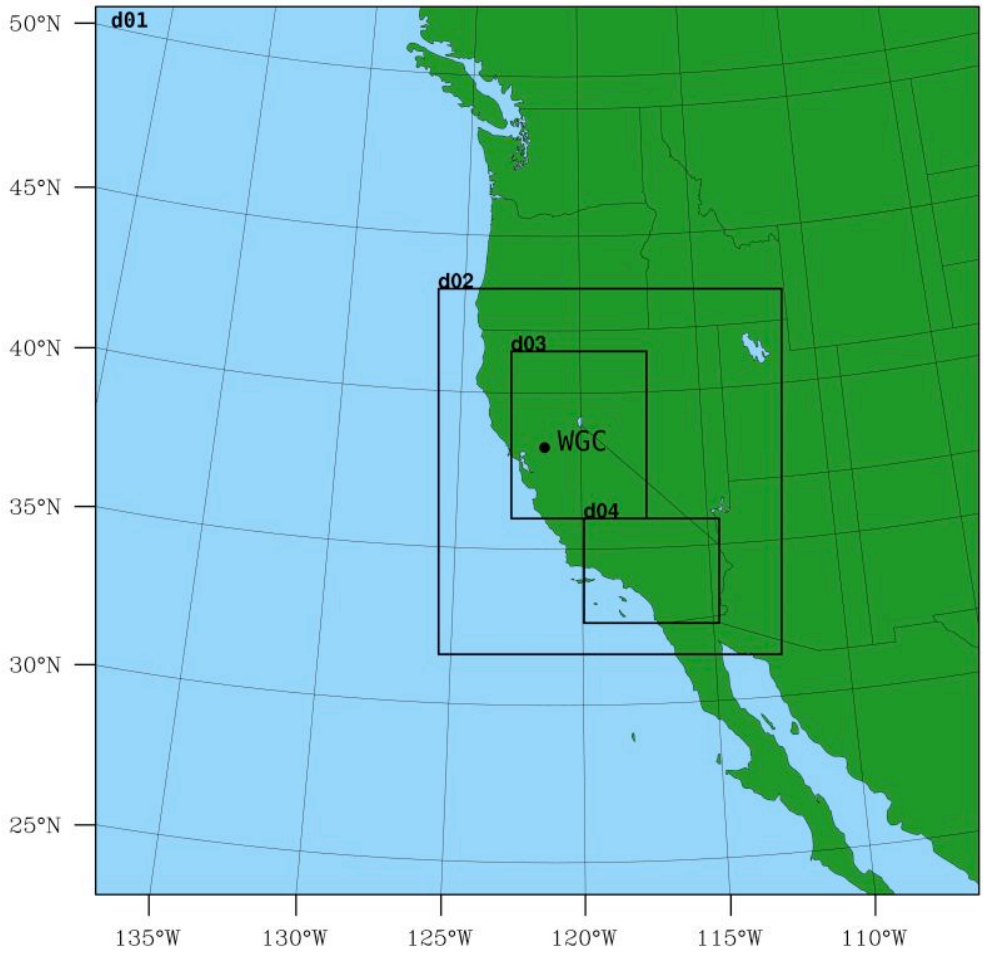

Figure 4. WRF initial boundary set up with three-level nested domains. The ratio of spatial resolution between the three levels is 3. The resolutions for d01, d02, d03 and d04 are 36, 12, 4 and 4 km, respectively.

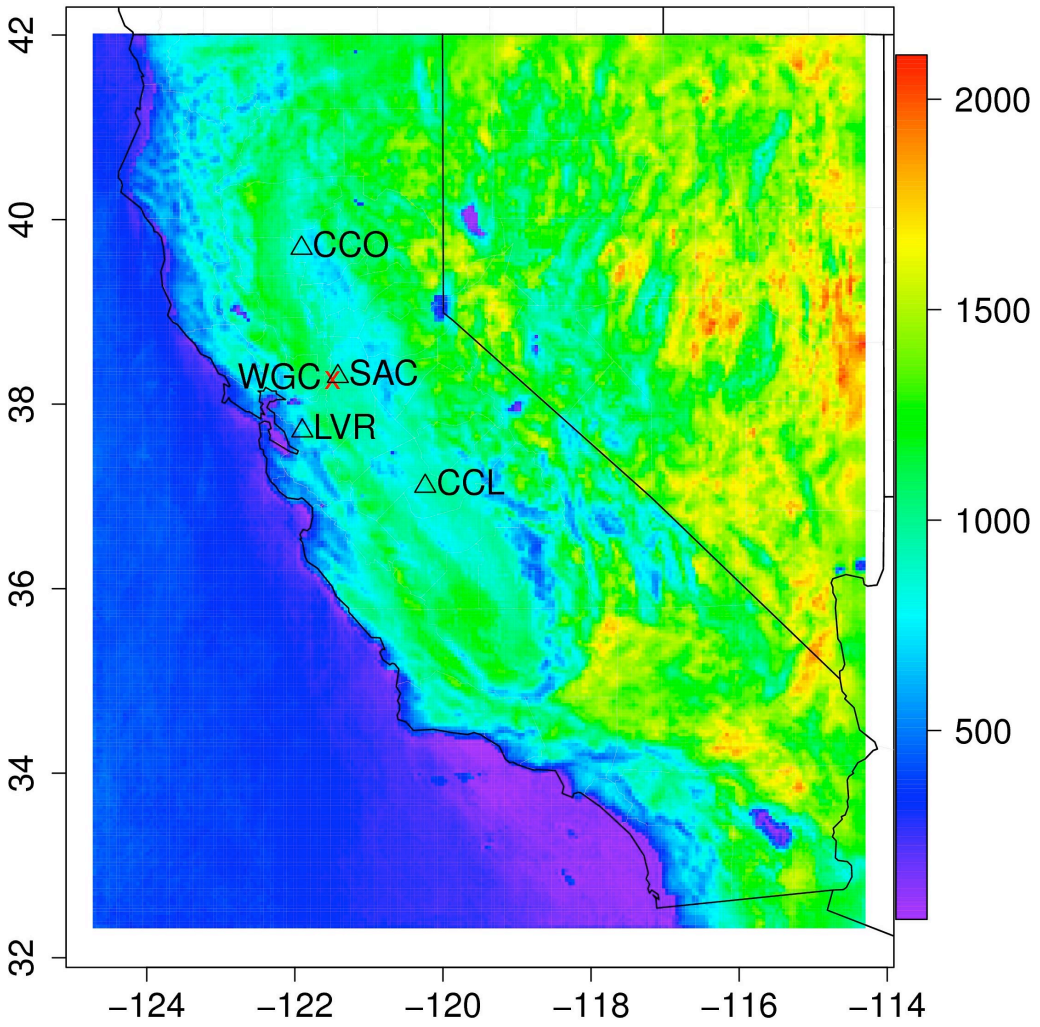

Figure 5. Map of Central California showing the location of Walnut Gove Tower (WGC; red "x") and the locations of the four radar wind profilers (black triangles) at Sacramento (SAC), Chico (CCO), Chowchilla (CCL) and Livermore (LVR), with predicted monthly mean PBL heights (m) for June 2008, 10:00 PST shown in color.

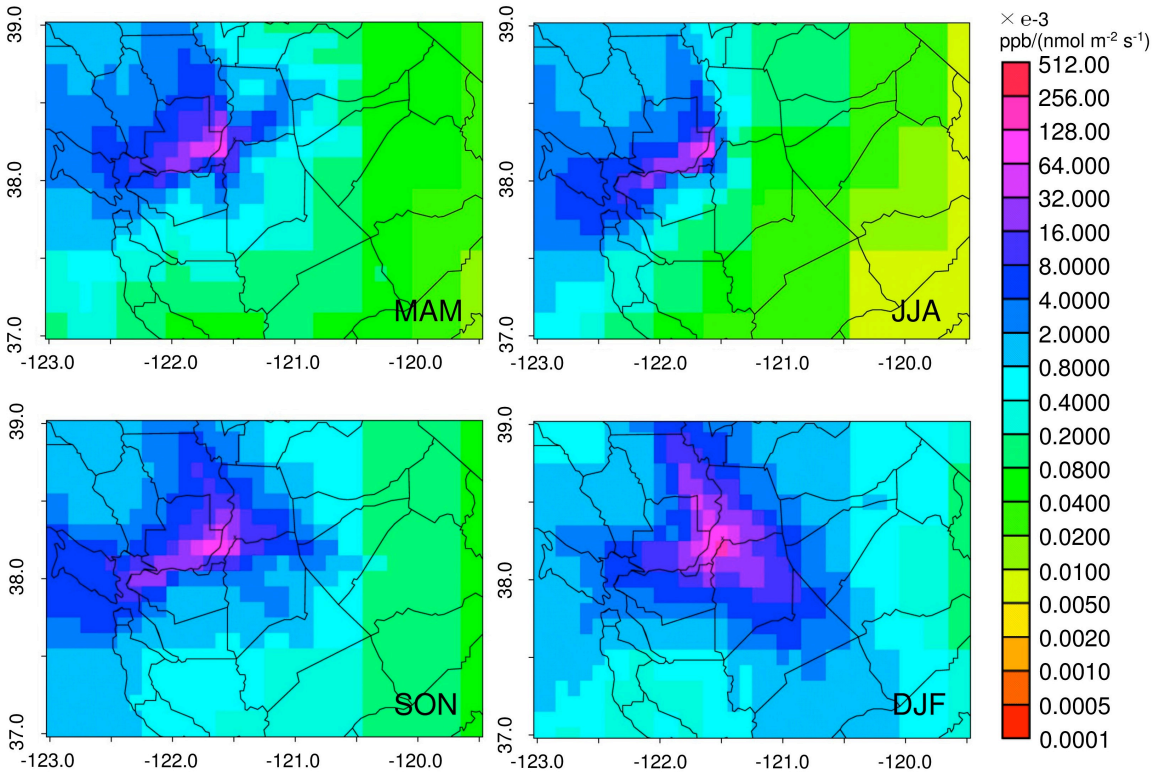

Figure 6. Seasonally averaged footprint maps over well-mixed periods for spring (MAM), summer (JJA), fall (SON), and winter (DJF).

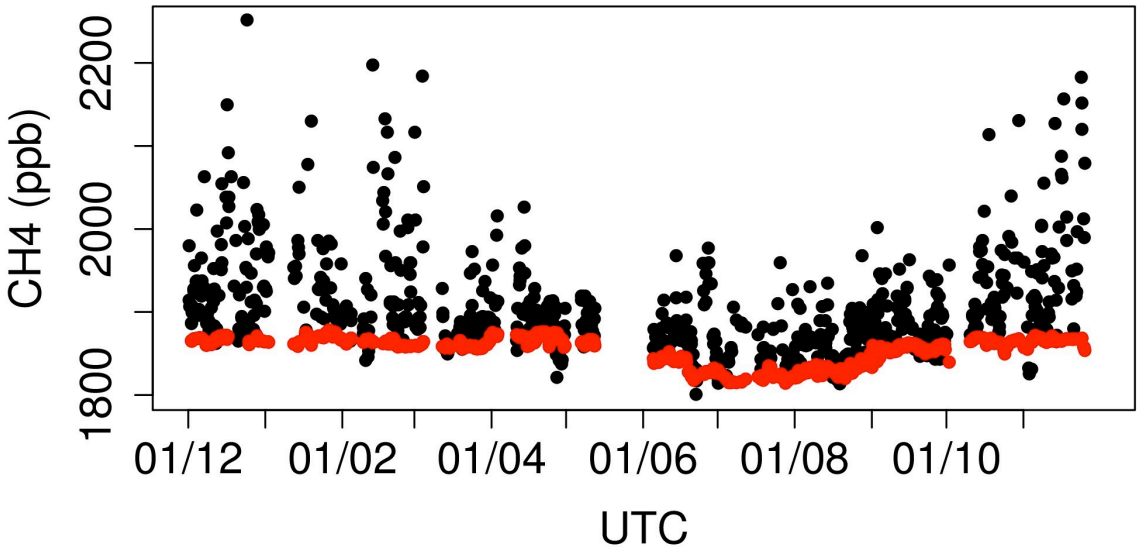

Figure 7. Time series (dates given as DD/MM) of measured CH_4 signals (black) and predicted background (red) CH_4 signals at 91 m on the WGC tower for well-mixed periods between December 1, 2007 and November 30, 2008.

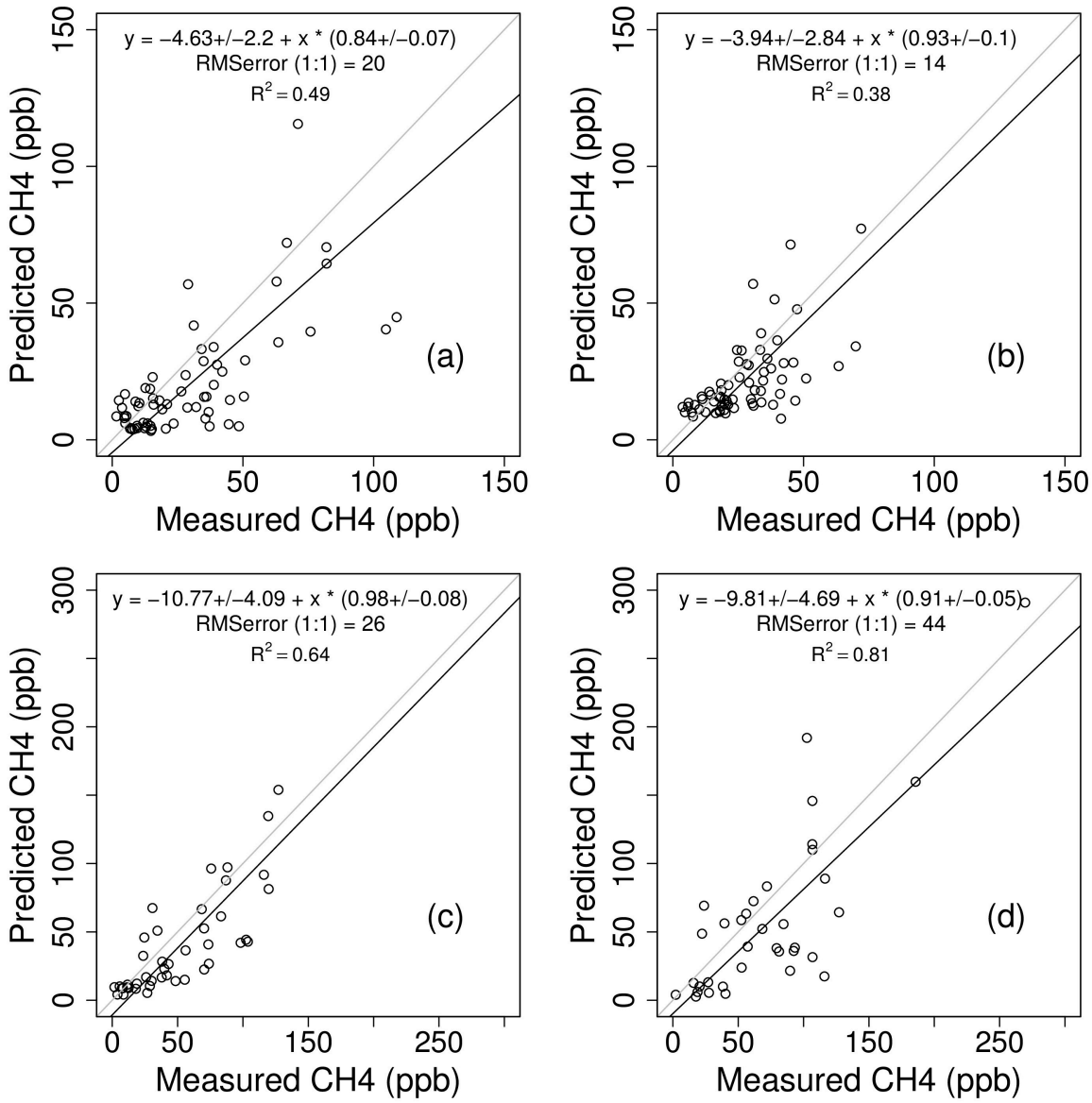

Figure 8. Comparison of CH_4 mixing ratios between measurements and predictions based on the final inverse optimization using CA-specific emissions for the mid-point month of (a) spring, (b) summer, (c) fall, and (d) winter. For summer, June and July mixing ratios are compared together due to data removal during fire periods.

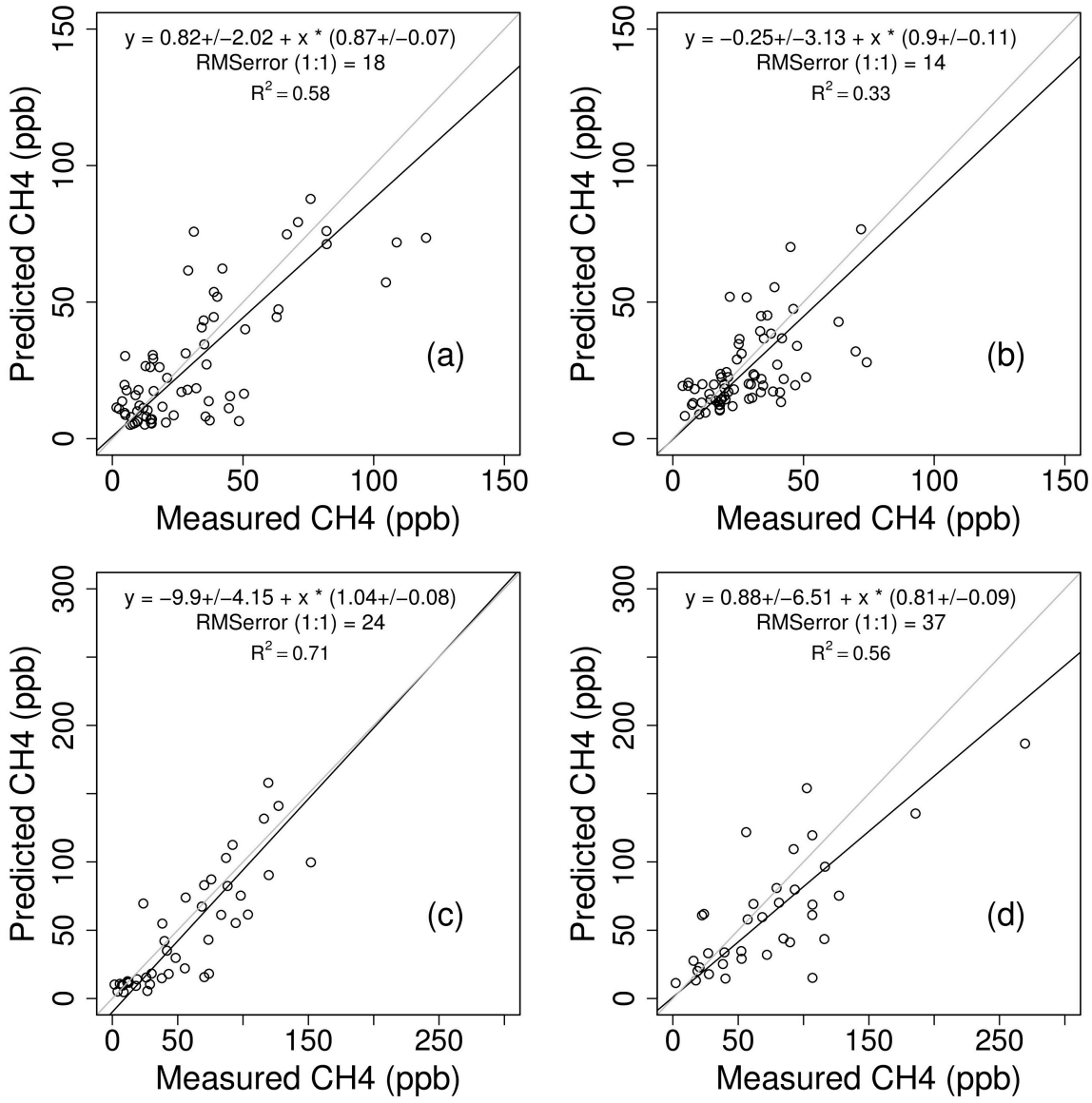

Figure 9. Comparison of CH_4 mixing ratios between measurements and predictions based on the final inverse optimization using EDGAR32 emissions for the mid-point month of (a) spring, (b) summer, (c) fall, and (d) winter. For summer, June and July mixing ratios are compared together due to data removal during fire periods.

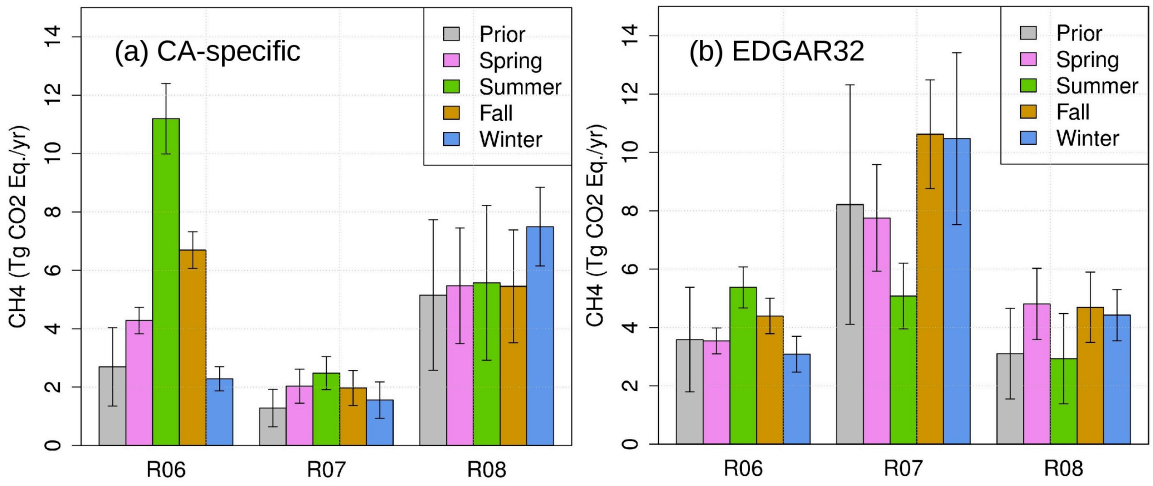

Figure 10. Comparison of posterior CH_4 emissions (Tg CO_2eq yr^{-1}, assuming a 100-year GWP = 21) by region between the (a) CA-specific and (b) EDGAR32 emission models.